# Robust Out-of-plane Rotation of Biological Cells Based on Polar Body Orientation Prediction

Huiying Gong, Yidi Zhang, Lu Zhou, *Member, IEEE*, Yaowei Liu, *Member, IEEE*, Qili Zhao, *Member, IEEE*, Xin Zhao, *Member, IEEE*, Mingzhu Sun*, *Member, IEEE*

***Abstract*—Three-dimensional rotation of the biological cell is essential for localizing subcellular structure in various cell manipulations. However, visual detection errors of the subcellular structure affect the rotation performance in automatic cell manipulations. In this paper, we enhance the robustness of out-of-plane rotation through visual detection evaluation. At first, we developed a kinematic model and simulation environment for cell rotation. We then predicted the presence and reliability of polar body detection using a posteriori probability analysis from 4 million simulations. We finally presented a robust out-of-plane rotation strategy based on polar body orientation prediction. Both simulation and experimental results with porcine oocytes demonstrated the efficiency and robustness of the proposed cell rotation method across various abnormal situations, improving the success rate of cell rotation. This work contributes a universal framework applicable to other vision-based cell rotation problems, offering a significant advancement in the field of cell manipulation.**

***Index Terms*—Biological cell manipulation, subcellular structure localization, cell rotation, polar body orientation prediction, visual detection evaluation.**

## I. Introduction

SUB-STRUCTURES within a cell have different functions, and when integrated, they form a complete cell. Three-dimensional rotation of the biological cell is essential for subcellular structure localization in various cell manipulations, such as intracytoplasmic sperm injection (ICSI) [1], [2], preimplantation genetic screening (PGS) [3], [4], preimplantation genetic diagnosis (PGD) [5], [6], somatic cell nuclear transfer (SCNT) [7], [8], and polar body genome transfer [9], [10]. In these cell surgery tasks, the specific subcellular structures are required to locate an appropriate orientation using noninvasive cell rotation. Take the polar body as an example, which is a kind of important subcellular structure and contains a copy of the genetic information of an oocyte or embryo. It is situated between the cytoplasm and zona pellucida inside the cell, as shown in Fig. 1. In the case of ICSI, the polar body should be rotated to the 9 or 12 o'clock position to avoid polar body damage; conversely, for SCNT, the polar body needs to be positioned at the 2 or 4 o'clock position to facilitate enucleation.

Huiying Gong, Yidi Zhang, Lu Zhou, Yaowei Liu, Qili Zhao, Xin Zhao and Mingzhu Sun are with the Institute of Robotics and Automatic Information System (IRAIS), the Tianjin Key Laboratory of Intelligent Robotic (tjKLIR), Nankai University, Tianjin 300350, China, the Institute of Intelligence Technology and Robotic Systems, Shenzhen Research Institute of Nankai University, Shenzhen, 518083, China.

This research was jointly supported by National Natural Science Foundation of China (62273185, 62333012) and Science and Technology Program of Tianjin (23JCYBJC01240).

*Contacting Author: Mingzhu Sun. (e-mail: sunmz@nankai.edu.cn)

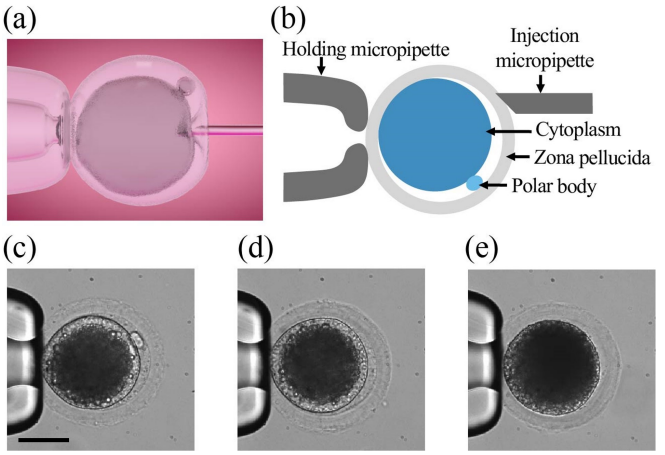


Fig. 1. Polar body of an oocyte/embryo. (a) 3D view of a cell with a polar body. The polar body is situated between the cytoplasm and zona pellucida inside the oocyte/embryo. The polar body should be rotated to the desired orientation for various cell surgery tasks. (b) The projection of the cell in the image plane. The polar body is visible when it is positioned near the image plane. (c) Porcine oocyte with the polar body visible in the image plane. (d) Porcine oocyte with the polar body outside the image plane. (e) Porcine oocyte without a polar body. Scale bar: 50$\mu$m

In the last two decades, cell rotation techniques have gained much attention. Cell rotation approaches can be divided into two main categories: physical contact approaches and non-contact approaches. In physical contact approaches, cells are immobilized using either a holding pipette [11]–[13] or an in-house developed holding stage [14], [15] . Orientation is achieved through friction between the cell and the injection pipette [16]–[18]. Some rotational or translational devices were also employed to rotate the cell by applying friction between the cell and the platform [19], [20]. Non-contact approaches include electric field-driven [21], [22], magnetic field-driven [23], [24], microfluidic flow [25], [26], optical tweezer [27], [28], acoustic field-driven [29], [30], etc. Ref. [31] has summarized the existing methods for cell orientation control. At present, both types of approaches have achieved cell rotation control with high precision and efficiency. Typically, the visual detection of the subcellular structure served as the control feedback to determine whether the rotation is complete.

As a kind of representative subcellular structure, polar body detection has been a focus of concern. Traditional image processing methods, such as thresholding segmentation, image texture detection, and contour curvature analysis [17], [20],

have been used to identify the polar body. While these methods are easily integrated into the micromanipulation system, their detection accuracy is significantly affected by the shape, size, and focus of the polar body, which can lead to inaccuracies and inefficiencies in certain conditions. Recently, there has been a shift towards more advanced object detection methods based on machine learning [32], [33] and deep learning [12], [34], [35] for detecting the polar body. These methods have shown effective and robust detection results, overcoming some of the limitations of traditional approaches. At the same time, it may require more computational resources and sophisticated training data, which could be a limitation in resource-constrained environments. Notably, in previous studies, we have achieved online detection of polar bodies from different animals with an average accuracy of 98 %, fulfilling the requirements for automatic cell rotation [36].

However, there are two primary issues with the aforementioned detection algorithms when applied to cell rotation. First, errors in visual detection have a significant impact on subsequent cell manipulations. The detection errors typically fall into two categories: false negative (FN), where the polar body present in the image is not detected; and false positive (FP), where the polar body is incorrectly identified in the image without a visible polar body. The FN case prolongs cell rotation time, potentially affecting cell viability. Conversely, in the FP case, it is mistakenly assumed that cell rotation has been completed and the subsequent procedure would be performed, ultimately resulting in the failure of cell manipulations.

Second, due to the imaging characteristics of the optical microscope, the polar body can only be visually recognized when it is near the image plane (Fig. 1(a-c)). Otherwise, it becomes defocused, merges with the cytoplasm, and becomes unobservable (Fig. 1(d)). The detection algorithms, and even human observers, struggle to differentiate between the absence of a polar body and a polar body that is out of the image plane (Fig. 1(d) and (e)). Regrettably, abnormal cellular development leads to some oocytes/embryos not having a polar body [37]. Due to the challenge of the target's initial position being unknown, robotic cell orientation techniques often involve an iterative process: the cell is continually rotated with a fixed or random rotational angle until the polar body is identified or it is concluded that the cell lacks a polar body. The process of cell rotation to bring the polar body into view is called "out-of-plane rotation". Current methods can only repeatedly rotate the cell to confirm the absence of a polar body during out-of-plane rotation, which significantly increases the operation time.

Out-of-plane rotation faces challenges due to the lack of effective visual feedback. Inaccuracy in visual detection greatly affects the reliability of cell manipulation. So far, few robotic or automatic cell manipulation methods have concentrated on evaluating the effectiveness of visual detection to enhance system robustness. In this study, we analyzed the patterns of polar body detection during cell rotation by combining a kinematic model and simulation of out-of-plane rotation, thereby obtaining the relationship between the rotational angle of the cell and the appearance orientation of the polar body. Utilizing this understanding, we designed a robust cell rotation strategy based on polar body orientation prediction.

The main contributions of this study are concluded as follows:

1) We established a theoretical kinematics model and developed a kinematic simulation environment for cell rotation. Using this model and environment, we could calculate the a posteriori probability of polar body appearance with the rotational angle of the cell and the orientation of the polar body.
2) We conducted millions of simulations and fulfilled the presence prediction of the polar body and reliability prediction for polar body detection based on a posteriori probability analysis of the simulation results.
3) We designed an out-of-plane rotation strategy based on polar body orientation prediction and validated the proposed strategy through the robotic rotation of porcine oocytes. The simulation and experimental results demonstrate the efficiency and robustness of the proposed method across various abnormal situations.

## II. Kinematic modeling and simulation

In cell manipulation, cells are usually immobilized and rotated using a holding pipette and an injection pipette respectively. The technologies reported in the literature have demonstrated high accuracy of cell rotation. Consequently, if the current position of the polar body and the rotation parameters are known, the 3D position of the polar body after cell rotation can be calculated. Building on this, we established a kinematic model for cell rotation and discussed the factors that affect the orientation of the polar body in the image.

### *A. Kinematic modeling for cell rotation*

In the kinematic model, the cell, the cytoplasm, and the polar body are modeled as spheres for simplicity, as the interactions between the micropipette and the cell surface are not considered. The origin of the local coordinate system is set to the center of the cell. Fig. 2(a) shows the spheres of the cytoplasm (the green solid line) and the polar body (the small blue solid sphere). The radii of the cytoplasm and the polar body are designated as $R_{cy}$ and $R_{pb}$, respectively. In Fig. 2(a), the blue-spotted sphere represents the 3D position of the polar body center. The polar body is constrained to move on this sphere, which has a radius of $C = R_{cy} + R_{pb}$. The polar body inclination angle $\phi$ is defined as the angle between the line connecting the polar body center to the origin and the $X-Y$ plane, with a range of $\phi \in (-180^\circ,\ 180^\circ]$. Supposing that the polar body distributes uniformly over the surface of the cytoplasm. Let the 3D coordinate of the polar body center be noted as $(x, y, z)$, then we have:

$$x^2 + y^2 + z^2 = C^2, \tag{1}$$

The inclination angle of the polar body is expressed as:

$$\phi = \begin{cases} \arccos(\sqrt{x^2+y^2}/C) & z \geq 0 \\ -\arccos(\sqrt{x^2+y^2}/C) & z < 0 \end{cases}, \tag{2}$$

The cytoplasm and polar body are projected onto the $X-Y$ plane, i.e. the image plane, as shown in Fig. 2(b). The distance

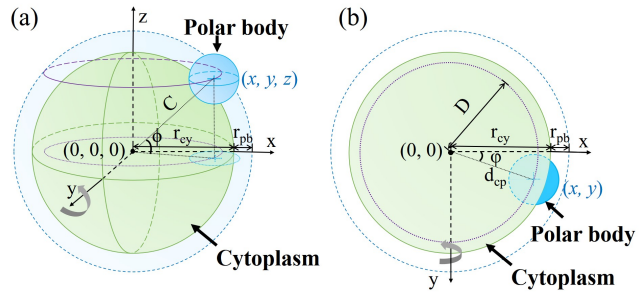


Fig. 2. The kinematic model for cell rotation. (a) 3D model of the cell. The origin of the local coordinate system is set to the center of the cell. The radii of the cytoplasm and the polar body are designated as $R_{cy}$ and $R_{pb}$. (b) The projection of the cell model in the $X-Y$ plane (the image plane). The distance from the center of the polar body to the origin in $X-Y$ plane is designated as $d_{cp}$.

from the center of the polar body to the origin in the $X-Y$ plane is designated as $d_{cp} = \sqrt{x^2+y^2}$. The orientation of the polar body $\varphi$ is defined as the angle between the line connecting the two centers and the positive direction of the X-axis, with a range of $\varphi \in (-180°,\ 180°]$:

$$\varphi = \begin{cases} \arccos(x/d_{cp}) & y \geq 0 \\ -\arccos(x/d_{cp}) & y < 0 \end{cases}, \tag{3}$$

Since the cytoplasm is not transparent, the polar body is considered to be visible in the image only when a small part or none of the polar body overlaps with the cytoplasm. Define parameter $D$ as the minimum distance from the polar body center to the origin in the $X-Y$ plane when the polar body is recognizable, as shown in the purple dotted circle in Fig. 2(b). The parameter $D$ is determined by the size of the polar body, $R_{cy} - R_{pb} < D \leq R_{cy} + R_{pb}$. The value of $D$ will be set according to the experimental observations.

If distance $d_{cp} < D$, the polar body is occluded by the cytoplasm. At this time, the cell needs to be rotated to make the polar body recognizable. Here, we have:

$$|z| = \sqrt{C^2 - {d_{cp}}^2} > \sqrt{C^2 - D^2}, \tag{4}$$

In other words, the polar body is unrecognizable when it is situated within the upper or lower spherical shells, as shown in Fig. 2(a).

Assuming that the cell can be rotated around any axis through the origin, we define the rotation axis as $\hat{K} = [k_x\ k_y\ k_z]^T$. If the polar body center initially lies at Point $P_0 = \begin{bmatrix} x_0 & y_0 & z_0 \end{bmatrix}^T$, after the cell rotates by an angle $\theta$ around the axis $\hat{K}$, the center will move to Point $P = \begin{bmatrix} x & y & z \end{bmatrix}^T$:

$$\begin{bmatrix} x\ y\ z \end{bmatrix}^T = \begin{bmatrix} k_xk_xv\theta + c\theta & k_xk_yv\theta - k_zs\theta & k_xk_zv\theta + k_ys\theta \\ k_xk_yv\theta + k_zs\theta & k_yk_yv\theta + c\theta & k_yk_zv\theta - k_xs\theta \\ k_xk_zv\theta - k_ys\theta & k_yk_zv\theta + k_xs\theta & k_zk_zv\theta + c\theta \end{bmatrix} \begin{bmatrix} x_0\ y_0\ z_0 \end{bmatrix}^T \tag{5}$$

where, $c\theta = \cos\theta, s\theta = \sin\theta, v\theta = 1 - \cos\theta$.

Since rotating the cell around the Z-axis does not alter the overlap area between the polar body and the cytoplasm in the $X-Y$ plane, for efficiency, the rotation axis should be positioned within the $X-Y$ plane through the origin. The rotation is the most effective when the rotation axis is perpendicular to the orientation of the polar body. Given that the position of the polar body is unknown, and the possibility of its orientation is the same, the rotation axis can be selected at random. For simplicity, we select the Y-axis as the rotation axis, denoted as $\hat{K}_Y = \begin{bmatrix} 0 & 1 & 0 \end{bmatrix}^T$.

### *B. Probability calculation of polar body appearance based on kinematic modeling*

To calculate the a posteriori probability of the polar body's appearance in the image, we perform a back-projection of the polar body region from the image plane onto the 3D surface of the cell and analyze the area on this 3D surface that the polar body may occupy.

There are two cases according to the visibility of the polar body. In case 1, the polar body is visible in the image after cell holding, which implies that the polar body is situated near the equator of the cell. Consequently, the cell does not need to be rotated. Assuming that the polar body is located in the region with the orientation $(\varphi_1, \varphi_2]$, this region is back-projected onto the 3D sphere with the area $S_0$. The area $S_0$ can be calculated as follows:

$$S_0(\varphi_1, \varphi_2) = \int_0^{\arccos\frac{D}{C}} 2 \cdot \cos\phi \cdot \mathrm{C}^2 \cdot (\varphi_2 - \varphi_1) \cdot d\phi, \tag{6}$$

where the integral variable $\phi$ represents the inclination angle of the polar body.

In case 2, the cell is rotated around the Y-axis to bring the polar body into view. Assuming the rotational angle is from $\theta_1$ to $\theta_2$, the newly observed area of the polar body with an orientation from $\varphi_1$ to $\varphi_2$ can be calculated by a double integral:

$$S_\theta(\theta_1, \theta_2, \varphi_1, \varphi_2) = \int_{\theta_1}^{\theta_2} \int_{\alpha(\varphi_1)}^{\alpha(\varphi_2)} h\left(\alpha, \theta\right) \cdot \cos\alpha \cdot C^2 \cdot d\alpha \cdot d\theta, \tag{7}$$

where the integral variable $\theta$ represents the rotational angle, $\alpha\left(\varphi\right)$ is an angle function related to the polar body orientation $\varphi$:

$$\alpha\left(\varphi\right) = \arcsin\frac{D \cdot \sin\varphi}{C}, \tag{8}$$

Function $h\left(\varphi, \theta\right)$ is a binary function related to the angles $\varphi$ and $\theta$, which represents whether there still exists an unobserved area in the orientation of $\varphi$ after a rotational angle of $\theta$:

$$h\left(\varphi, \theta\right) = \begin{cases} 1 & 2 \cdot \arcsin\left(\frac{\sqrt{D^2 - (C \cdot \sin\alpha(\varphi))^2}}{\sqrt{C^2 - (C \cdot \sin\alpha(\varphi))^2}}\right) > \theta \\ 0 & others \end{cases}, \tag{9}$$

Please refer to the Supplementary Material for further details on the derivation of Eq. (6) and (7).

Combining Eqs. (6) and (7), the posteriori probability of the new appearance within the orientation range $(\varphi_1, \varphi_2]$ after rotating the cell by the angle from $\theta_1$ to $\theta_2$ can be expressed:

$$P\left(\theta_1,\theta_2,\varphi_1,\varphi_2\right)=\frac{S\left(\theta_1,\theta_2,\varphi_1,\varphi_2\right)}{S_{spere}}, \tag{10}$$

where, $S_{spere}=4\pi C^2$ is the surface area of the 3D sphere where the polar body moves. $S$ represents all possible positions of the polar body on the sphere:

$$S\left(\theta_1,\theta_2,\varphi_1,\varphi_2\right)=\begin{cases} S_0\left(\varphi_1,\varphi_2\right) & \theta_1=\theta_2=0 \\ S_\theta\left(\theta_1,\theta_2,\varphi_1,\varphi_2\right) & \text{others} \end{cases}. \tag{11}$$

### *C. Probability estimation of polar body appearance based on kinematic simulation*

There are numerous uncertainties in cell rotation, such as the difference between the actual and set rotational angle, and variations in the sizes of the polar bodies. We further employed the kinematic simulation of cell rotation to model the uncertainties and estimate the appearance probability of the polar body.

In the kinematic simulation, the actual rotational angle of the cell was modeled to follow a normal distribution, with a mean equal to the set value and a standard deviation of 10%, based on experimental observations. The rotation was incremented in units of 10°, which means we assess whether the polar body appears in the image plane using the visual algorithms every 10° of cell rotation. The increment ensures that the polar body will be not missed due to the excessive rotation. Since the stochastic nature of the cell's orientation during micropipette aspiration, the polar body is randomly initialized with a uniform distribution at any orientation on the surface of the sphere. Based on the characteristics of the porcine oocytes, the radius of the polar body $R_{pb}$ is statistically approximately 0.17 times that of the cytoplasmic radius $R_{cy}$. Therefore, the radius of the polar body was set according to a normal distribution with a mean value of $0.17R_{cy}$ and a standard deviation of 10%. Meanwhile, the polar body is considered visible when at least one-third of its area appears in the image plane. This criterion implies a minimum distance of $D=R_{cy}-0.27R_{pb}$ from the polar body center to the origin, which is calculated based on geometric relationships. Fig. 3 shows the 3D visualization (Fig. 3(a-c)) and the corresponding image plane projections (Fig. 3(d-f)) of the cell rotation kinematic simulation. As the cell rotates, the potential regions where the polar body can be located (the purple region in Fig. 3(a-c)) diminish in size, transforming the presence of the polar body in the cell from a probabilistic event to a deterministic one.

To verify the kinematic simulation, the cell rotation simulation was conducted 100,000 times, with the polar body randomly distributed each time. The rotational angle of the cell and the orientation of the polar body were recorded when the polar body appeared in the image. Fig. 4(a) shows the posteriori probability of the polar body appearance, where the X-axis and Y-axis represent the rotational angle of the cell and the orientation of the polar body at the moment of appearance, respectively. Since the rotation angle of 0° implies that the polar body is already situated in the image plane without cell rotation, this situation is not shown in the figure for better visualization. For statistical analysis, the appearance orientation of the polar body is divided into 36 intervals, each spanning 10° . The same rotation and oocyte shape parameters were input into Eq. (11) to theoretically calculate a posterior probability of the polar body appearance. As shown in Fig. 4, the results from the kinematic simulation are consistent with the theoretical calculations, validating the effectiveness of the simulation model.

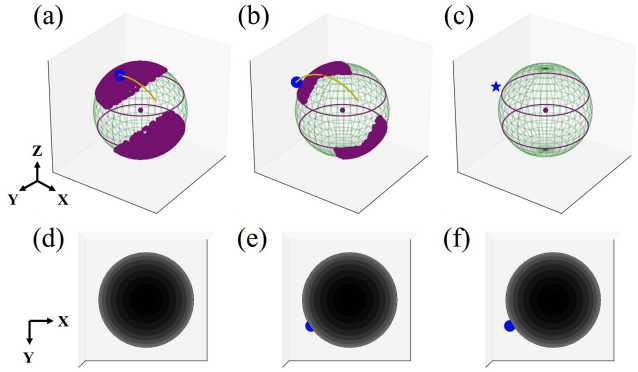


Fig. 3. Kinematic simulation of cell rotation. (a-c) 3D model of the cell. The green sphere and the small blue sphere represent the cytoplasm and the polar body, respectively. The purple circle represents the boundary between the visible and invisible spherical shell regions of the polar body in the image plane. The purple area represents the current possible spherical shell region of the polar body. As the cells rotate, more of the spherical shell regions are observed in the image plane, so the purple area correspondingly reduces in size. (d-f) The corresponding projection of the cell model in the image plane. The black circle and the small blue circle represent the cytoplasm and the polar body, respectively.

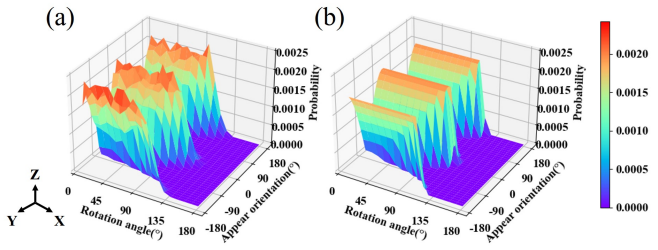


Fig. 4. A posteriori probability of polar body appearance with the rotational angle of the cell and the orientation of the polar body. (a) Kinematic simulation results. (b) Theoretical calculation results.

## III. Polar Body Orientation Prediction Based on Kinematic Simulation

Based on the analysis in the preceding section, it is evident that the appearance orientation of the polar body correlates with the rotation angle during the rotation process. Further considering practical cell manipulations, it is laborious to ensure the presence of polar bodies in all oocytes to be operated. Moreover, visual detection errors are inevitable during cell rotation. Consequently, the actual cell rotation process cannot be accurately simulated by the theoretical model alone.

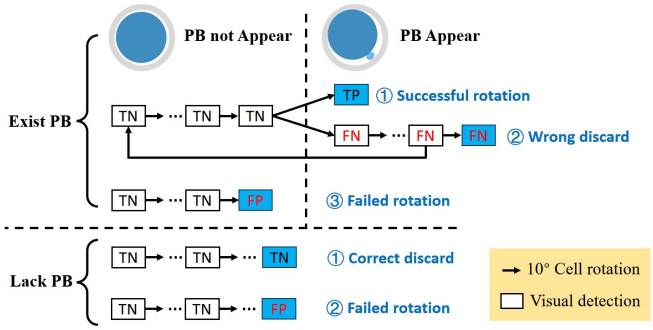


Fig. 5. Possible rotation results in cell rotation simulation.

To address these issues, we utilized kinematic simulation to analyze and predict the orientation of the polar body.

### A. Kinematic simulation setup

According to the extensive statistics in our oocyte vitro maturation experiments, we made a generalizing assumption that 80% of the oocytes had polar bodies. We also considered two types of polar body visual detection errors: FP and FN. FPs occur when a polar body is falsely detected in images lacking a polar body, while FNs occur when a polar body is missed in images where it is present. In our rotation simulation, visual detection was conducted after every 10° increment of cell rotation.

Under the above setting, the possible rotation results are shown in Fig. 5 according to the presence of polar bodies and the occurrence of visual detection errors. The arrows and boxes represent 10° increments of cell rotation and the results of visual detection, respectively. Within the boxes, TP (true positive) and TN (true negative) refer to correct visual detection results, indicating correct detections of images with or without a polar body.

When an oocyte contains a polar body, which is assumed to be randomly distributed, three cases may occur:

- If the visual detection is correct after each rotation, a series of TNs followed by a TP once the polar body becomes visible, resulting in a successful rotation.
- If the visual detection is correct before the polar body appears, but an FN occurs when the polar body does appear and FN continues, the rotation is considered complete after a full-circle rotation. In this case, we incorrectly conclude that the cell lacks a polar body, leading to a wrong discard of the cell.
- If an FP occurs during cell rotation, the rotation is wrongly considered completed, resulting in a failed rotation.

When the oocyte lacks a polar body, two cases may occur:

- If the visual detection is correct after each rotation, a series of TNs until the cell has completed a full rotation, resulting in a correct discard.
- If an FP occurs before a full-circle rotation, the rotation is wrongly considered complete, leading to a failed rotation.

The simulation results vary with differing FP and FN rates. In the case of FNs, the wrong discard of cells with the polar body occurs only when continuous FNs happen, which is very rare. For FP cases, the proportion of failed rotations is highly sensitive to the FP rate, as a single FP occurrence can immediately result in failed rotations. Therefore, we should focus on analyzing failed rotations due to visual FPs.

In this study, we set 6 different FP rates: 0.01, 0.02, 0.05, 0.1, 0.2, and 0.3, which were selected based on recent reports of polar body detection accuracies. For consistency, the FN rates were set equal to the corresponding FP rates. A total of 4,700,000 simulations were conducted across these conditions. After each simulation, we recorded the cell rotational angle and the orientation of the polar body. Different from cell experiments, in the simulation environment, it is straightforward to differentiate between the real successful/failed rotations and correct/wrong discards. We counted all successful and failed rotation samples at the interval of 10° for both cell rotational angle and orientation of the polar body. The statistics results were recorded in two matrices $\mathbf{SR}$ and $\mathbf{SR}$. Specifically, $\mathbf{SR}^r_{a,o}$ and $\mathbf{FR}^r_{a,o}$ represent the number of successful and failed rotation samples, respectively, for a given rotation angle range $(a-10°, a]$ and polar body orientation range $(o-10°, o]$ at an FP rate $r$, where $a \in \{10°, ..., 180°\}$, and $o \in \{-170°, -160°, ..., 0, 10°, ...180°\}$. Especially, $\mathbf{SR}^r_{0,o}$ and $\mathbf{FR}^r_{0,o}$ represent the samples without any cell rotation. We predicted the presence of the polar body and assessed the detection reliability of the polar body according to the statistics.

### B. Presence prediction of the polar body

To predict the presence of the polar body, we focused on the simulation results of all successful rotations. We calculated the cumulative probability of successful rotations $P^r_{cu\_SR}(a, o)$ for a given rotation angle $a$ and polar body orientation $o$ at an FP rate $r$ according to Eq. (12):

$$P^r_{cu\_SR}(a,o) = \frac{\sum_{i=0}^{a/10} \mathbf{SR}^r_{10\cdot i,o}}{\sum_{i=0}^{18}\sum_{j=-17}^{18} \mathbf{SR}^r_{10\cdot i,10\cdot j}}, \tag{12}$$

Taking the FP rate of 0.05 as an example, Fig. 6(a) shows the cumulative posterior probability $P^{0.05}_{cu\_SR}(a, o)$, where the X-axis and Y-axis represent the cell rotational angle and the orientation of the polar body when the rotation is complete. The probability of successful rotation increases as the cell undergoes further rotation.

Moreover, we summarized the relationship between the cell rotational angle and the cumulative posterior probability $P^r_{cu\_SR\_a}(a)$ of rotation success under various FP rates according to Eq. (13):

$$P^r_{cu\_SR\_a}(a) = \frac{\sum_{i=0}^{a/10}\sum_{j=-17}^{18} \mathbf{SR}^r_{10\cdot i,10\cdot j}}{\sum_{i=0}^{18}\sum_{j=-17}^{18} \mathbf{SR}^r_{10\cdot i,10\cdot j}}. \tag{13}$$

As shown in Fig. 6(b), all existing polar bodies become visible in the $X-Y$ plane by rotating the cell with a maximum of

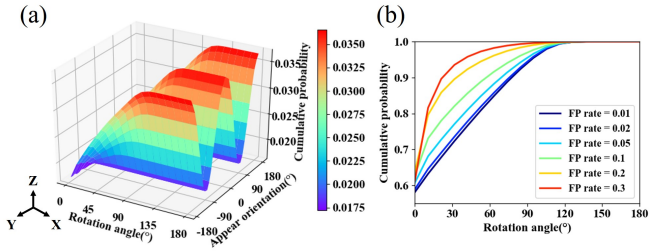


Fig. 6. Cumulative posterior probability of all successful rotations. (a) Cumulative posterior probability $P^{0.05}_{cu\_SR}(a,o)$ at an FP rate of 0.05. (b) Cumulative posterior probability $P^{r}_{cu\_SR\_a}(a)$.

140°. Consequently, if the polar body is not observed after the cell has been rotated by 140°, it can be concluded that the cell does not contain a polar body.

### C. Reliability prediction for polar body detection

We analyzed all the simulation results of both successful and failed rotations to predict the detection reliability of the polar body. Initially, we calculated the probability of the successfully rotated samples $P^{r}_{SR}(a,o)$ for a given rotation angle $a$ and polar body orientation $o$ at an FP rate $r$ relative to all samples, according to Eq. (14):

$$P^{r}_{SR}(a,o)=\frac{\mathbf{SR}^{r}_{a,o}}{\sum_{i=0}^{18}\sum_{j=-17}^{18}\mathbf{SR}^{r}_{10\cdot i,10\cdot j}+\sum_{i=0}^{18}\sum_{j=-17}^{18}\mathbf{FR}^{r}_{10\cdot i,10\cdot j}}, \tag{14}$$

Fig. 7(a) shows the probability distribution of the successful rotations at an FP rate of 0.05 as an example, where the X-axis and Y-axis represent the cell rotational angle and the orientation of the polar body, respectively. The situation without cell rotation is not shown in the figure for better visualization. The probabilities of the polar body appearing vary across different orientations. Specifically, the probabilities of the pole body appearing at 0° and ±180° are much greater than those at orientations near ±90°.

Moreover, we summarized the relationship between the polar body orientation and the rotation success probability at an FP rate $r$. The cumulative probability of successful rotations $P^{r}_{SR\_o}(o)$ can be computed using Eq. (15):

$$P^{r}_{SR\_o}(o)=\frac{\sum_{i=0}^{18}\mathbf{SR}^{r}_{10\cdot i,o}}{\sum_{i=0}^{18}\sum_{j=-17}^{18}\mathbf{SR}^{r}_{10\cdot i,10\cdot j}+\sum_{i=0}^{18}\sum_{j=-17}^{18}\mathbf{FR}^{r}_{10\cdot i,10\cdot j}}, \tag{15}$$

Fig. 7(b) shows the rotation success probability under various FP rates. As the FP rate decreases, the distribution of the polar body orientation becomes increasingly evident.

Similarly, we calculated the probability of failed rotation samples relative to all samples $P^{r}_{FR}(a,o)$ and cumulative probability of failed rotations $P^{r}_{FR\_o}(o)$, according to Eq. (16) and (17). Fig. 7(c) and (d) show the probability distributions

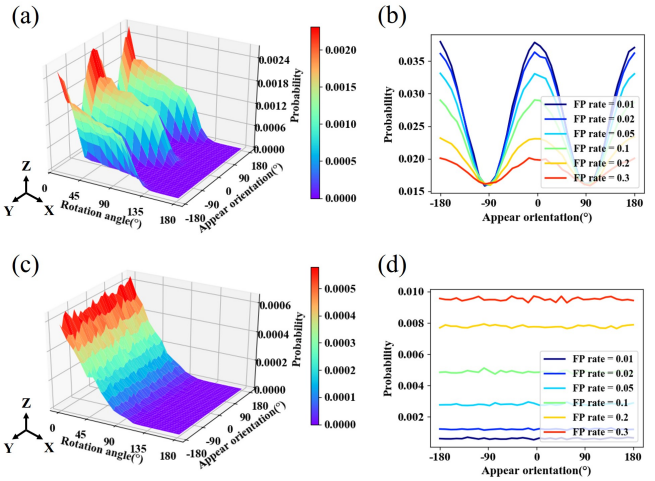


Fig. 7. Probability distribution of successful and failed rotations. (a) Probability of successful rotation samples relative to all samples $P^{0.05}_{SR}(a,o)$ at an FP rate of 0.05. (b) Cumulative probability of successful rotations $P^{r}_{SR\_o}(o)$. (c) Probability of failed rotation samples relative to all samples $P^{0.05}_{FR}(a,o)$ at an FP rate of 0.05. (d) Cumulative probability of failed rotations $P^{r}_{FR\_o}(o)$.

at an FP rate of 0.05 and under varying FP rates, respectively. Given that the polar body is randomly distributed in the cell, the probabilities of the polar body appearing are uniform across different orientations. As the FP rate increases, the probability of the failed rotation also increases.

$$P^{r}_{FR}(a,o)=\frac{\mathbf{FR}^{r}_{a,o}}{\sum_{i=0}^{18}\sum_{j=-17}^{18}\mathbf{SR}^{r}_{10\cdot i,10\cdot j}+\sum_{i=0}^{18}\sum_{j=-17}^{18}\mathbf{FR}^{r}_{10\cdot i,10\cdot j}}, \tag{16}$$

$$P^{r}_{FR\_o}(o)=\frac{\sum_{i=0}^{18}\mathbf{FR}^{r}_{10\cdot i,o}}{\sum_{i=0}^{18}\sum_{j=-17}^{18}\mathbf{SR}^{r}_{10\cdot i,10\cdot j}+\sum_{i=0}^{18}\sum_{j=-17}^{18}\mathbf{FR}^{r}_{10\cdot i,10\cdot j}}, \tag{17}$$

We integrated the simulation results of both successful and failed rotations to calculate the probability of the failed rotations $P^{r}_{fail}(a,o)$ across different rotation angles and polar body orientations according to Eq. (18).

$$P^{r}_{fail}(a,o)=\frac{\mathbf{FR}^{r}_{a,o}}{\mathbf{SR}^{r}_{a,o}+\mathbf{FR}^{r}_{a,o}}. \tag{18}$$

Fig. 8 shows the probability distributions of the failed rotations $P^{r}_{fail}(a,o)$ at FP rates of 0.01, 0.02, and 0.05, respectively. $P^{r}_{fail}(a,o)$ is significantly higher at orientations near ±90° than at 0° and ± 180°. This is because failed rotations are independent of the orientation of the polar body, while the successful rotations depend on that angle, as shown in Fig. 7(b) and (d). Specifically, detection results at the orientations of ±90° are incorrect because the polar body will not appear there. Additionally, as the FP rate increases, the overall probability distributions for failed rotations also increase. Since failed rotations are caused by visual detection

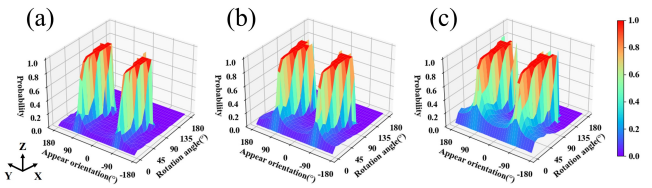


Fig. 8. Probability distribution of the failed rotations $P^r_{fail}(a, o)$ at FP rates of (a) 0.01, (b) 0.02 , and (c) 0.05.

errors, $P^r_{fail}(a, o)$ serves as an indicator of the detection reliability for a given rotation angle $a$ and orientation $o$.

### D. Out-of-plane rotation strategy

Through previous theoretical analysis and simulation statistics, we have determined that the appearance of the polar body is related to the rotation angle of the cell and the orientation of the polar body, despite the random distribution of the polar body. Based on these findings, we draw the following conclusions.

1) The rotation axis should lie within the $X-Y$ plane and pass through the origin to maximize the efficiency of polar body localization.
2) It is only necessary to rotate the cell around the rotation axis by 140° to ascertain if the cell contains a polar body. This eliminates the need for repeated rotation, thereby reducing the time required for confirmation.
3) The detection reliability could be utilized to reduce the incidence of failed rotations due to visual false detections of the polar body, leading to a more stable rotation process.

For Point 3, the FPs in the polar body detection are often caused by impurities that are precisely located between the cytoplasm and the transparent band. If the cell is re-rotated and the image is captured again for re-detection, it will help mitigate the impact of the initial FP. Consequently, we determined whether to perform a second detection based on the reliability of the polar body detection. Additionally, considering that a higher FP rate correlates with more frequent detection errors, continuous re-detection may only prolong the rotation process without significantly improving the success rate of rotation if the FP rate is low. Ultimately, we adopted a second detection only in situations where the detection reliability falls within a predetermined range. Based on the probability of the failed rotations $P^r_{fail}(a, o)$ in Eq. (18), the detection reliability is classified into three categories:

- If $P^r_{fail}(a, o)$ is less than twice the FP rate in the polar body detection, the detection is deemed reliable. It is concluded the polar body has been successfully identified, and the out-of-plane rotation is terminated.
- If $P^r_{fail}(a, o)$ is higher than 0.9, the detection is deemed unreliable. It is concluded that the visual detection is likely incorrect, no polar body is present in the image, and further rotation is necessary.
- If $P^r_{fail}(a, o)$ lies between twice the FP rate in the polar body detection and 0.9, the detection is considered suspicious and a second detection is conducted.

We have designed an out-of-plane rotation strategy, as shown in Fig. 9. We set the rotation axis to the Y-axis based on Point 1 and performed polar body detection while cell rotation. If the polar body was not detected, the cell was rotated by 10° and the detection continued. If the polar body remained unidentified after a total rotation of 140°, meaning that all regions on the cell surface have been inspected according to Point 2, the cell was determined to lack a polar body and was discarded. Once the polar body was detected, we assessed the detection reliability. For situations deemed suspicious according to Point 3, we re-rotated the cell of 20° and conducted a second detection. If it was ultimately determined that the polar body was identified, the out-of-plane rotation was completed.

Specifically, before the cell rotation process, a pre-experiment was conducted on the cell samples to statistically assess the FP rate of the visual detection algorithm. If the detection algorithm is modified or changes occur in the cell state or liquid environment, the pre-experiment is repeated to update the FP rate. Simulated detection reliability data corresponding to various FP rates were pre-stored in a table. This table was used for real-time lookup during the cell rotation process based on the current FP rate. For real-time polar body detection, we utilized a U-net-based image recognition method as described in Ref. [36]. In this experiment, detection reliability data with an FP rate of 0.02 was used.

Cell rotation was performed using a pair of glass micropipettes (holding and injection micropipettes) without additional equipment. We employed trajectory planning based on the minimum rotation force [11] and the optimal poking direction [13] of the injection micropipette to ensure effective cell rotation, as illustrated in Fig. 10. The oocyte was immobilized on the holding micropipette with negative pressure, and the injection micropipette tip was positioned 50 $\mu$m from the zona pellucida along the X-axis (Point A). The oocyte's position and radius were obtained using Canny edge detection and Hough circle detection, while the injection micropipette tip was located via template matching. Next, the injection micropipette moved along the Z-axis to the start position (Line A-B) for out-of-plane rotation. Point B was located above the imaging plane at $\mathrm{R}\cdot\cos\theta_{in}$, where R is the cell radius and $\theta_{in}$ is the initial angle. It then pokes the cell along the negative X-axis (Line B-C) and pull the cell to rotate along an arc (Arc C-D) with a contact angle $\Delta\theta$. The micropipette returned to the start position via Lines D-E and E-B. During Arc C-D, the poking depth was dynamically calculated based on the oocyte's mechanical properties and the micropipette's orientation [11]. Finally, this B-C-D-E-B trajectory was repeated cyclically for continuous cell rotation at a speed of 100 $\mu$m/s.

## IV. Simulation and Experimental Results

### A. Simulation Results

We conducted simulations to evaluate the proposed strategy by testing three types of out-of-plane rotation strategies in the simulation environment. The strategies evaluated were: the one-shot detection strategy which detects the polar body only once, the universal re-detection strategy which re-confirms the detection of the polar body every time, and the proposed

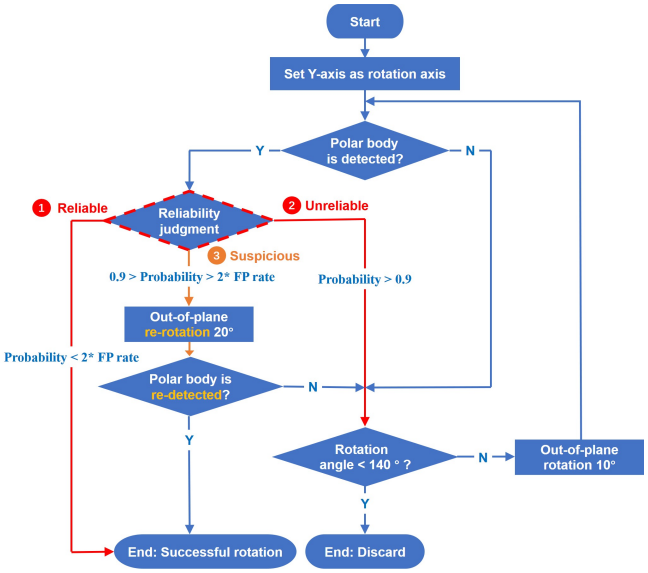


Fig. 9. Out-of-plane rotation strategy based on polar body orientation prediction.

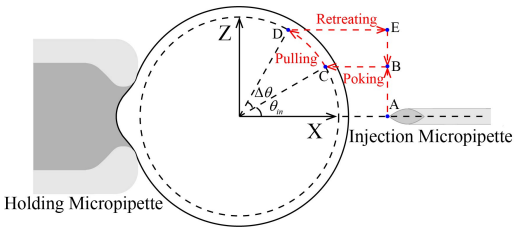


Fig. 10. Out-of-plane rotation control method.

strategy which decides whether to re-detect the polar body based on its detection reliability. In simulations, the detection reliability was calculated using the lookup table of the simulation statistical results. The re-rotation angle was set to 20° to ensure that the polar body would not disappear due to excessive rotation and to maintain visual differences in the images before and after re-detection.

We performed 6,000,000 rotation simulations on oocytes with polar bodies at 7 different FP rates ranging from 0.01 to 0.3. Fig. 11(a) shows that the average rotation success rate decreases for all strategies as the FP rate increases, but the decline varies. Both the proposed and universal re-detection strategies consistently outperform the one-shot strategy. At an FP rate of 0.05, the proposed strategy achieves a 92.9% success rate, 3% higher than the one-shot strategy's 89.9%, effectively reducing the FP impact to an equivalent rate of 0.03. These results indicate that the proposed and universal strategies both enhance the robustness against FP-related errors than the one-shot strategy. However, Fig. 11(b) illustrates that compared to the one-shot strategy, both the proposed and universal re-detection strategies require additional rotation angles to achieve higher success rates.

To quantify the trade-off between success rate improvement and additional rotation of the proposed and the universal re-detection strategy, we defined the rotation efficiency as the

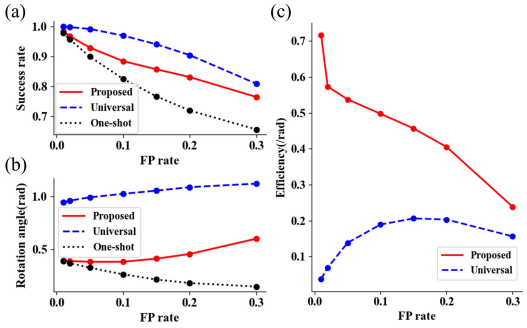


Fig. 11. (a) Average rotation success rate, (b) average rotation angle and (c) rotation efficiency for the proposed strategy, one-shot detection strategy, and universal re-detection strategy respectively under varying FP rates.

ratio of success rate improvement to the increased rotation angle (rad) compared to the one-shot strategy. As shown in Fig. 11(c), the proposed strategy achieves significantly higher rotation efficiency than the universal re-detection strategy across all FP rates. This demonstrates that the proposed strategy not only achieves a high success rate but also minimizes additional rotation, effectively balancing robustness and efficiency.

### B. Experimental setup

As shown in Fig. 12, the micromanipulation system used to perform our designed cell rotation method consists of the following facilities: an inverted microscope (Ti-E, Nikon) equipped with an $X-Y$ motorized stage (ProScan III, Prior). The cell samples, placed in a 35mm petri dish on the $X-Y$ stage, are manipulated by a holding micropipette (70$\mu$m in outer diameter and 30$\mu$m in inner diameter) and a sharpened injection micropipette (25$\mu$m in diameter). These two micropipettes are mounted on motorized $X-Y-Z$ micromanipulators (MP285, Sutter), offering a motion range of 25mm and a positioning resolution of 0.04$\mu$m. A motorized syringe is connected to the holding micropipette for cell aspiration. Additionally, a CCD camera (acA645-100gm, Basler) is mounted on the microscope to capture images at 30 frames/s.

In the experiment, mature porcine oocytes were prepared as follows: Porcine ovaries were collected from the local slaughterhouse, and the oocytes were aspirated from follicles (2-6mm in diameter) using a syringe. Subsequently, these oocytes were matured in vitro for 42 hours to reach maturity. All oocytes were tested within 4 hours of delivery and were stored in a 37°C environment.

### C. Experimental results

In the cell rotation experiment, the proposed rotation strategy was evaluated 100 times by using 20 porcine oocytes. Specifically, 17 oocytes containing polar bodies were rotated 90 times, while 3 oocytes lacking a polar body were rotated 10 times. Consistent with the conditions of real biological experiments, we did not pre-screen the cells, so there were more impurities around the oocyte, as shown in Fig. 13. The polar bodies were initially distributed randomly before each rotation. When the out-of-plane rotation stopped, we

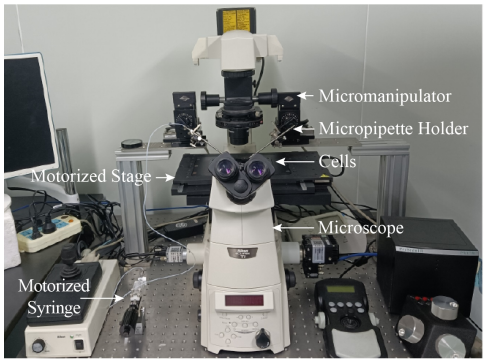


Fig. 12. System setup for cell rotation experiment.

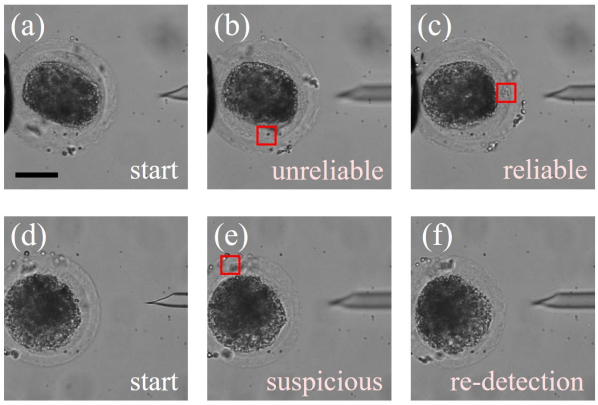


Fig. 13. Cell rotation results based on the proposed out-of-plane rotation strategy. (a-c) A cell rotation with unreliable detection due to impurities. (d-f) A cell rotation with suspicious detection and re-detection. Scale bar: 50$\mu$m

considered a rotation successful if the majority of the polar body was visible in the image plane. Meanwhile, we deemed a rotation a correct discard if a cell without a polar body was accurately identified and the rotation was stopped promptly. We used a holding pressure of 1600 Pa, with the poking depth during rotation kept below 15$\mu$m. To assess the impact of rotation on cell viability, all oocytes were carefully examined under high magnification ($\times$20 objective lens) after rotation. The observations showed no observable morphological damage. Furthermore, FDA fluorescence staining was conducted for viability evaluation, revealing no significant difference in fluorescence intensity compared to the unmanipulated control group (results shown in the Supplementary Material), confirming that the operation caused minimal damage.

Fig. 13 shows the cell rotation results employing the proposed out-of-plane rotation strategy. In one rotation sequence in Fig. 13(a-c), an impurity (the red box in Fig. 13(b)) is located at the orientations of 90°. Given the low visual detection reliability at this orientation, the detection is deemed unreliable and the cell needs to continue rotating. In the following rotation, the rotation is considered terminated once the detection reliability is sufficiently high, as shown in Fig. 13(c). Fig. 13(d-f) shows another instance of cell rotation. In Fig. 13(e), the detection reliability falls into the suspicious range, thus an additional rotation is performed for re-detection. As the polar body is not detected for the second time after cell rotation, as shown in Fig. 13(f), the previous detection is deemed incorrect and the rotation process continues.

Out of 90 rotations of porcine oocytes with polar bodies, 76 were successful, yielding a success rate of 84.4%. The failed rotations were mainly attributed to visual detection errors, which included 4 FN cases and 10 FP cases. The average time and rotation angle for out-of-plane rotation of cells were about 5.9s and 47.1°, respectively, with a maximum rotation angle of 100° in successful cases. Among the 10 rotations of the oocytes lacking a polar body, only one rotation failed due to false detection, and the remaining 9 tests successfully terminated after a 140° rotation. The whole cell rotation process took 13.3 seconds on average. Table 1 shows the comparison between the proposed method and existing methods. The proposed method improved the success rate of out-of-plane rotation of cells containing polar bodies with only a small increase in time. Additionally, for cells without a polar body, the proposed method provided more accurate and fast criteria for judgment, improving the rotation efficiency significantly.

TABLE I
COMPARISON BETWEEN THE PROPOSED METHOD AND OTHER PUBLISHED CELL ROATION METHODS

| Polar body existence | Method | Success Rate | Operation Time |
|---|---|---|---|
| Existent | Gong's [36] | 80% | 5.5s |
| | Ours | 84.4% | 5.9s |
| Non-existent | Wang's [17] | - | 15 rounds |
| | Gong's [36] | - | 30s |
| | Leung's [38] | - | 30s |
| | Ours | 90% | 13.34s |

### D. Discussion

In this study, the effectiveness of the proposed out-of-plane rotation strategy was verified through the porcine oocyte rotation experiments. Compared to other types of oocytes commonly used in experiments, such as human and mouse oocytes, porcine oocytes have a smaller proportion of polar bodies, which are often completely occluded by the opaque cytoplasm. This makes the out-of-plane rotation of porcine oocytes particularly challenging. The proposed strategy is particularly useful for this task due to its robustness in visual detection. Although when the FP rate of the visual detection algorithm is high, relying solely on the proposed re-detection strategy is insufficient to achieve a satisfactory rotation success rate. In such cases, improving the detection algorithm accuracy itself becomes a more effective solution. However, it is worth noting that this method constitutes a universal framework, and can be flexibly applied to other vision-based rotation problems by simply changing the shape and rotation parameters in the simulation, improving the effectiveness of rotation.

In the experiment, out of 90 rotations, approximately 500 detections were conducted, with 14 FPs and 4 FNs. The average accuracy of online polar body detection was 96.5%, slightly lower than the pre-experiment results of 98%. Specifically, 14 FPs were primarily attributed to the impurities of the oocytes. Among them, 10 FPs resulted in failed rotations, while the other 4 FPs were successfully identified by the proposed strategy. There were also 4 rotation failures caused by FNs, all of which occurred because the polar bodies were too small to be recognized in multiple visual detections.

It is important to note that, despite the polar body detection accuracy exceeding 96%, the final success rate of out-of-plane rotation was only 84.4%. Although this represents a 4% improvement over the detection results in Ref. [36], there was still significant room for improvement. In the future, we will consider the temporal correlation between consecutive FPs and FNs in experiments, introduce confidence analysis from the image detection neural network, and explore optimizations in hardware design and the rotation control algorithm. This probably further improves the success rate and efficiency of the rotation system.

## V. Conclusion

Three-dimensional rotation of the biological cell is crucial for subcellular structure localization in various cell manipulations. In which, out-of-plane rotation faces challenges due to the lack of effective visual feedback. In this paper, we developed a kinematic cell rotation model and analyzed the reliability of polar body detection based on the model. Furthermore, we designed a robust cell rotation strategy based on polar body orientation prediction. This work is the first evaluation of visual detection during automatic cell manipulations.

To verify the proposed cell rotation strategy, a total of 6,000,000 rotation simulations were performed on the oocytes with polar bodies at different FP rates. The proposed strategy successfully balanced the rotation success rate with rotation efficiency. Moreover, we conducted 100 out-of-plane rotation experiments using 20 porcine oocytes, which was particularly challenging due to the small size and occlusion of the polar bodies in the porcine oocytes. The rotation success rate was 84.4%, which represented a 4% improvement over the previous detection results, indicating the effectiveness of the proposed method. In the future, we aim to enhance cell rotation performance by incorporating temporal correlation analysis in continuous visual detection.

## References


[1] L. Yang, F. Liang, R. Zhu, Q. Wang, L. Yao, and X. Zhang, "Efficacy of intracytoplasmic sperm injection in women with non-male factor infertility: A systematic review and meta-analysis," *Acta Obstetricia et Gynecologica Scandinavica*, vol. 103, no. 1, pp. 30–41, 2024.

[2] W. Hu, H. Liang, J. Li, Z. Zhan, Y. Zhang, and C. Hu, "Three-dimensional positioning of the micropipette for intracytoplasmic sperm injection," in *2021 IEEE International Conference on Robotics and Automation (ICRA)*. IEEE, 2021, pp. 1249–1255.

[3] J. C. Harper, "Preimplantation genetic screening," *Journal of medical screening*, vol. 25, no. 1, pp. 1–5, 2018.

[4] V. S. Jiang and C. L. Bormann, "Non-invasive genetic screening: current advances in artificial intelligence for embryo ploidy prediction," *Fertility and Sterility*, 2023.

[5] O. El Tokhy, M. Salman, and T. El-Toukhy, "Preimplantation genetic diagnosis," *Obstetrics, Gynaecology & Reproductive Medicine*, vol. 31, no. 6, pp. 157–161, 2021.

[6] A. Alteri, G. C. Cermisoni, M. Pozzoni, G. Gaeta, P. I. Cavoretto, and P. Viganò, "Obstetric, neonatal, and child health outcomes following embryo biopsy for preimplantation genetic testing," *Human reproduction update*, vol. 29, no. 3, pp. 291–306, 2023.

[7] P. Mrowiec and M. Bugno-Poniewierska, "Technical, biological and molecular aspects of somatic cell nuclear transfer–a review," *Annals of Animal Science*, vol. 22, no. 1, pp. 63–87, 2022.

[8] A. Swegen, R. Appeltant, and S. A. Williams, "Cloning in action: can embryo splitting, induced pluripotency and somatic cell nuclear transfer contribute to endangered species conservation?" *Biological Reviews*, vol. 98, no. 4, pp. 1225–1249, 2023.

[9] H. Ma, R. C. O'Neil, N. M. Gutierrez, M. Hariharan, Z. Z. Zhang, Y. He, C. Cinnioglu, R. Kayali, E. Kang, Y. Lee *et al.*, "Functional human oocytes generated by transfer of polar body genomes," *Cell stem cell*, vol. 20, no. 1, pp. 112–119, 2017.

[10] T. Wang, H. Sha, D. Ji, H. L. Zhang, D. Chen, Y. Cao, and J. Zhu, "Polar body genome transfer for preventing the transmission of inherited mitochondrial diseases," *Cell*, vol. 157, no. 7, pp. 1591–1604, 2014.

[11] Q. Zhao, M. Sun, M. Cui, J. Yu, Y. Qin, and X. Zhao, "Robotic cell rotation based on the minimum rotation force," *IEEE Transactions on Automation Science and Engineering*, vol. 12, no. 4, pp. 1504–1515, 2014.

[12] C. Dai, Z. Zhang, Y. Lu, G. Shan, X. Wang, Q. Zhao, C. Ru, and Y. Sun, "Robotic manipulation of deformable cells for orientation control," *IEEE Transactions on Robotics*, vol. 36, no. 1, pp. 271–283, 2019.

[13] C. Zhao, Y. Liu, M. Sun, and X. Zhao, "Robotic cell rotation based on optimal poking direction," *Micromachines*, vol. 9, no. 4, p. 141, 2018.

[14] X. Liu, Z. Lu, and Y. Sun, "Orientation control of biological cells under inverted microscopy," *IEEE/ASME Transactions on Mechatronics*, vol. 16, no. 5, pp. 918–924, 2010.

[15] Z. Lu, X. Zhang, C. Leung, N. Esfandiari, R. F. Casper, and Y. Sun, "Robotic icsi (intracytoplasmic sperm injection)," *IEEE Transactions on Biomedical Engineering*, vol. 58, no. 7, pp. 2102–2108, 2011.

[16] R. Mori, T. Aoyama, T. Kobayashi, K. Sakamoto, M. Takeuchi, and Y. Hasegawa, "Real-time spatiotemporal assistance for micromanipulation using imitation learning," *IEEE Robotics and Automation Letters*, vol. 9, no. 4, pp. 3506–3513, 2024.

[17] Z. Wang, Y. Hu, J. Wei, and W. T. Latt, "Visual servoed robotic mouse oocyte rotation," *IEEE Transactions on Biomedical Engineering*, vol. 67, no. 8, pp. 2389–2396, 2019.

[18] H. Gong, Y. Zhang, Y. Liu, Q. Zhao, X. Zhao, and M. Sun, "Automatic cell rotation method based on deep reinforcement learning," in *2023 IEEE International Conference on Robotics and Automation (ICRA)*. IEEE, 2023, pp. 5452–5458.

[19] I. Abu Ajamieh, B. Benhabib, and J. K. Mills, "Automatic system for the blastocyst embryo manipulation and rotation," *Annals of biomedical engineering*, vol. 48, no. 1, pp. 426–436, 2020.

[20] S. Cui and W. T. Ang, "Robotic micromanipulation of biological cells with friction force-based rotation control," in *2020 IEEE/RSJ International Conference on Intelligent Robots and Systems (IROS)*. IEEE, 2020, pp. 2792–2798.

[21] K. Huang, I. A. Ajamieh, Z. Cui, J. Lai, J. K. Mills, and H. K. Chu, "Automated embryo manipulation and rotation via robotic ndep-tweezers," *IEEE Transactions on Biomedical Engineering*, vol. 68, no. 7, pp. 2152–2163, 2020.

[22] L. Huang, W. He, and W. Wang, "A cell electro-rotation micro-device using polarized cells as electrodes," *Electrophoresis*, vol. 40, no. 5, pp. 784–791, 2019.

[23] G. Lin, Y. Liu, G. Huang, Y. Chen, D. Makarov, J. Lin, Z. Quan, and D. Jin, "3d rotation-trackable and differentiable micromachines with dimer-type structures for dynamic bioanalysis," *Advanced Intelligent Systems*, vol. 3, no. 2, p. 2000205, 2021.

[24] F. Berndt, G. Shah, R. M. Power, J. Brugués, and J. Huisken, "Dynamic and non-contact 3d sample rotation for microscopy," *Nature communications*, vol. 9, no. 1, pp. 1–7, 2018.

[25] X. Liu, Y. Li, L. Li, M. Kojima, Q. Shi, Q. Huang, T. Fukuda, and T. Arai, "Noncontact 3-d orientation control at microscale: Hydrodynamic out-of-plane rotation and in-plane rotation by compacted rotational stage," *IEEE/ASME Transactions on Mechatronics*, 2022.

[26] X. Liu, Q. Shi, Y. Lin, M. Kojima, Y. Mae, T. Fukuda, Q. Huang, and T. Arai, "Multifunctional noncontact micromanipulation using whirling flow generated by vibrating a single piezo actuator," *Small*, vol. 15, no. 5, p. 1804421, 2019.

[27] J. Sun, N. Koukourakis, J. Guck, and J. W. Czarske, "Rapid computational cell-rotation around arbitrary axes in 3d with multi-core fiber," *Biomedical Optics Express*, vol. 12, no. 6, pp. 3423–3437, 2021.

[28] M. Xie, "Autonomous robot-aided optical tweezer system for biological cell manipulation," *The International Journal of Advanced Manufacturing Technology*, vol. 105, no. 12, pp. 4953–4966, 2019.

[29] J. Zhu, Q. Zhang, F. Liang, Y. Feng, and W. Wang, "High-throughput acoustofluidic microchannels for single cell rotation," *Journal of Micromechanics and Microengineering*, vol. 31, no. 12, p. 124004, 2021.

[30] L. Huang, F. Liang, Y. Feng, P. Zhao, and W. Wang, "On-chip integrated optical stretching and electrorotation enabling single-cell biophysical analysis," *Microsystems & Nanoengineering*, vol. 6, no. 1, pp. 1–14, 2020.

[31] T. Tang, Y. Hosokawa, T. Hayakawa, Y. Tanaka, W. Li, M. Li, and Y. Yalikun, "Rotation of biological cells: fundamentals and applications," *Engineering*, 2021.

[32] S. Asadzadeh, S. Daneshvar, B. Abedi, B. S. Oskouei, P. Shahabi, and Y. Jasemian, "Technical report: An advanced algorithm for the description of mice oocyte cytoplasm and polar body," *Biomedical Signal Processing and Control*, vol. 48, pp. 171–178, 2019.

[33] D. Meyer, M. L. P. Colon, H. V. Alizadeh, L. Su, B. Behr, and D. B. Camarillo, "Orienting oocytes using vibrations for in-vitro fertilization procedures," in *2019 International Conference on Robotics and Automation (ICRA)*. IEEE, 2019, pp. 4837–4843.

[34] Y. Wang, Y. Liu, M. Sun, and X. Zhao, "Deep-learning-based polar-body detection for automatic cell manipulation," *Micromachines*, vol. 10, no. 2, p. 120, 2019.

[35] Z. Yongxing, L. Liqun, L. Juan, W. Huiquan, and Z. Dan, "A real-time oocyte polar body detection method," in *Journal of Physics: Conference Series*, vol. 1754, no. 1. IOP Publishing, 2021, p. 012219.

[36] H. Gong, L. Li, J. Qiu, Y. Yao, Y. Liu, M. Cui, Q. Zhao, X. Zhao, and M. Sun, "Automatic cell rotation based on real-time detection and tracking," *IEEE Robotics and Automation Letters*, vol. 6, no. 4, pp. 7909–7916, 2021.

[37] T. Ebner, C. Yaman, M. Moser, M. Sommergruber, O. Feichtinger, and G. Tews, "Prognostic value of first polar body morphology on fertilization rate and embryo quality in intracytoplasmic sperm injection," *Human Reproduction*, vol. 15, no. 2, pp. 427–430, 2000.

[38] C. Leung, Z. Lu, X. P. Zhang, and Y. Sun, "Three-dimensional rotation of mouse embryos," *IEEE Transactions on Biomedical Engineering*, vol. 59, no. 4, pp. 1049–1056, 2012.


**Huiying Gong** received the bachelor's degree in automation from the Taiyuan University of Technology, Shanxi, China, in 2019. She is currently pursuing the Ph.D. degree with the School of Artificial Intelligence, Nankai University, Tianjin, China. Her current research interests include micromanipulators and microscope image processing.

**Yidi Zhang** was born in 1997. She received the bachelor's degree in automation from the Hebei University of Technology, Tianjin, China, in 2019. She is currently pursuing the Ph.D. degree with the School of Artificial Intelligence, Nankai University, Tianjin. Her current research interests include micromanipulation and micro- and nanorobotics.

**Lu Zhou** (Member, IEEE) received the B.S. degree in computer science and technology (with honors) and the M.S. degree in control science and engineering from Nankai University, Tianjin, China, in 2008 and 2011, respectively. She is currently an Associate Professor of laboratory technology with the Institute of Robotics and Automatic Information Systems, Nankai University, Tianjin, China. Her research interests include artificial intelligence and robotics, virtual reality, and intelligent simulation.

**Yaowei Liu** (Member, IEEE) received the B.Eng. degree in automation and the Ph.D. degree in control theory and control engineering from Nankai University, Tianjin, China, in 2013 and 2019, respectively. He finished his post-doctoral research with the College of Artificial Intelligence, Nankai University in 08/2023. He is currently an Assistant Professor with the College of Artificial Intelligence, Nankai University. His research interests include robotic cell micromanipulation and robotic cell measurement.

**Qili Zhao** (Member, IEEE) received the Ph.D. degree in control theory and control engineering from Nankai University, Tianjin, China, in 2014. He finished his first post-doctoral research with the Robotics and Mechatronics Research Laboratory, Department of Mechanical and Aerospace Engineering, Monash University, Melbourne, VIC, Australia, in 2015. He was a Post-Doctoral Fellow with the Advanced Micro and Nanosystems Laboratory, Department of Mechanical and Industrial Engineering, Toronto University, Toronto, ON, Canada, from 2015 to 2018. He is currently an Assistant Professor with the College of Artificial Intelligence, Nankai University. His research interests include automated drug screen, robotic beating heart cells manipulation system, robotic cell manipulation, and robotic cell measurement.

**Xin Zhao** (Member, IEEE) received the B.S. degree in control theory and control engineering from Nankai University, Tianjin, China, in 1991, the M.S. degree in control theory and control engineering from the Shenyang Institute of Automation, CAS, Shenyang, China, in 1994, and the Ph.D. degree in control theory and control engineering degree from Nankai University in 1997. He joined the faculty at Nankai University in 1997, where he is currently a Professor and the Dean of the College of Artificial Intelligence. His current research interests include micromanipulator, microsystems, and mathematical biology.

**Mingzhu Sun** (Member, IEEE) received the B.S. degree in computer science and technology, the M.S. degree in computer application, and the Ph.D. degree in control theory and control engineering from Nankai University, Tianjin, China, in 2003, 2006, and 2009, respectively. She joined the faculty at Nankai University in 2009, she is currently a Professor and the Deputy Director of the Institute of Robotics and Automatic Information System. Her research interests are in micromanipulator, image processing, and computer vision.